THE ASTROPHYSICAL JOURNAL, 445:599–606, 1995 June 1

THE SPATIAL VARIATION OF THE INFRARED-TO-RADIO RATIO IN SPIRAL GALAXIES

K. A. MARSH
Jet Propulsion Laboratory, California Institute of Technology, MS 306-451, 4800 Oak Grove Drive, Pasadena, CA 91109
AND
G. HELOU
Infrared Processing and Analysis Center, California Institute of Technology, IPAC 100-22, Pasadena, CA 91125
Received 1994 September 20; accepted 1994 December 12

ABSTRACT

We have produced two-dimensional maps of the intensity ratio, Q_{60}, of 60 μm infrared to 20 cm radio continuum emission, for a set of 25 nearby galaxies, mostly spirals. The ratio maps were obtained from infrared images made using *IRAS* data with the maximum correlation method, and radio images made using VLA data. Before taking the ratio, the radio images were processed so as to have the same resolution properties as the infrared images; the final spatial resolution in all cases is approximately 1′, corresponding to 1–2 kpc for most galaxies. This resolution represents a significant improvement over previous studies.

Our new high-resolution maps confirm the slow decrease of Q_{60} with increasing radial distance from the nucleus, but show additional structure which is probably associated with separate sites of active star formation in the spiral arms. The maps show Q_{60} to be more closely related to infrared surface brightness than to the radial distance r in the galaxy disk. We note also that the Q_{60} gradients are absent (or at least reduced) for the edge-on galaxies, a property which can be attributed to the dilution of contrast due to the averaging of the additional structure along the line of sight.

The results are all in qualitative agreement with the suggestion that the radio image represents a smeared version of the infrared image, as would be expected on the basis of current models in which the infrared-radio correlation is driven by the formation of massive stars, and the intensity distribution of radio emission is smeared as a result of the propagation of energetic electrons accelerated during the supernova phase.

Subject headings: galaxies: photometry — galaxies: sprial — infrared: galaxies — radio continuum: galaxies

1. INTRODUCTION

Observations of spiral galaxies at far-infrared and centimeter wavelengths have revealed a strong correlation between the flux densities in these two regimes (Dickey & Salpeter 1984; de Jong et al. 1985; Helou, Soifer, & Rowan-Robinson 1985; Sanders & Mirabel 1985). The correlation appears to hold for all galaxies whose far-infrared luminosities are dominated by ongoing star formation, including ellipticals with hidden star-forming disks (Wrobel & Heeschen 1988) and distant starburst galaxies at $z > 0.1$ and $L_{\rm FIR} > 10^{11}\ L_\odot$ (Karoji, Dennefeld, & Ukita 1985). This was unexpected, since different mechanisms are responsible for the infrared and radio emission; the infrared represents thermal emission from heated dust, while the radio is dominated by nonthermal synchrotron emission, even though thermal bremsstrahlung plays an important role at frequencies above about 5 GHz (Price & Duric 1992).

Naturally, the result prompted comparisons between the spatial structure of galaxy disks at infrared and radio wavelengths. A close correspondence has been found between the spatial appearance of spiral galaxies in these two wavelength regimes (Wunderlich & Klein 1988; Wainscoat, de Jong, & Wesselius 1987), although the infrared-to-radio intensity ratio appears to be enhanced in the central regions (Beck & Golla 1988; Bicay, Helou, & Condon 1989). More recently, Bicay & Helou (1990, hereafter BH90) compared the spatial distributions, at 60 μm and 20 cm wavelengths, for 25 galaxies (24 late-type spirals and one irregular), and found that the radio images had the appearance of smeared versions of the infrared images.

The above studies have suggested that the underlying link between infrared and radio emission involves the formation of relatively massive ($\gtrsim 5\ M_\odot$) stars, which heat the infrared-emitting dust and then accelerate the synchrotron-emitting electrons during the subsequent supernova phase. On the question of why the infrared-radio correlation should be so tight, Helou & Bicay (1993) have suggested that this comes about because the dust-heating photons and relativistic electrons are generated in the same proportions in all galaxies, and there is a close coupling between magnetic field strength and gas density. An alternative explanation has been advanced by Bettens et al. (1993), who have invoked a feedback mechanism in which the cosmic-ray electrons (generated by the supernova) influence the subsequent star formation rate in molecular clouds, via ionization effects. For any of these models, the smearing of the radio images finds a natural explanation in terms of the propagation of the synchrotron-emitting electrons before they are subsequently lost to radiative decay or escape (BH90).

The infrared images on which the BH90 study was based were derived directly from the raw detector data from the *Infrared Astronomical Satellite* (*IRAS*), which were of rather coarse spatial resolution (1.′5 × 4.′7). Since the latter dimension was comparable to the sizes of the galaxies themselves, the study was basically one-dimensional in terms of spatial resolution. In this paper we describe an improved approach to the study of the spatial properties of the infrared-radio correlation using infrared data of higher spatial resolution ($\sim 1'$ in both coordinates).

2. DATA

The galaxy sample used in the current investigation consisted of the same 25 galaxies studied by BH90. Our input data for each galaxy consisted of the following:

1. Radio continuum image at 20 cm wavelength (frequency 1.49 GHz) made using the VLA, and described by Condon (1987). The CLEAN algorithm was applied to the maps, with circular Gaussian restoring beams of FWHM 0.'8, 0.'9, or 1.'0.

2. Infrared continuum image at 60 μm wavelength, made using data from *IRAS*, and the imaging technique known as the maximum correlation method (MCM), described by Aumann, Fowler, & Melnyk (1990). The number of iterations used was 20.

Although the infrared and radio images had comparable spatial resolution ($\sim 1'$), the infrared images were non-isoplanatic. The behavior of their resulting point-spread functions (PSFs) was determined by the *IRAS* scanning geometry, the spatial responses of the set of *IRAS* detectors that scanned the source, and the inherent properties of the MCM. Since the goal of the study was to compare radio and infrared images at the same spatial resolution, further processing was necessary.

3. ANALYSIS PROCEDURE

In order to produce pairs of images (radio and infrared) with the same spatial resolution, we re-CLEANed the radio images and restored them using an effective PSF corresponding to the infrared images. The procedure involved the following steps:

1. Deconvolve the radio PSF. This step was necessary, since the original sets of CLEAN components involved in Condon's (1987) maps were not available. The deconvolution was performed by a reapplication of the CLEAN algorithm, based on the same circular Gaussian beam which Condon had used to restore each map. The image was CLEANed down to the residual noise level (0.1 mJy beam^{-1}), yielding a source model in the form of a set of delta-function components.

2. Generate synthetic "raw detector data" such as would be observed if this source model were scanned using detectors whose spatial responses were the same as for *IRAS*, and using the same scanning geometry as for the original *IRAS* observations.

3. Run these data through the same MCM imaging algorithm as was used to generate the infrared images. The pixel size (15″), field of view, and position of the center pixel were the same as for the corresponding infrared image.

Since the CLEANing operation introduces a small degree of additional smoothing to the radio image as a result of the discretization of component locations, some compensating smoothing was necessary for the infrared image. The form of the smoothing function, whose width was a small fraction of a pixel, was determined numerically. Having applied this compensation, the result in each case was a radio image whose spatial resolution properties were essentially identical to that of the corresponding infrared image.

Because of uncertainties in the absolute positioning of the *IRAS* data (resulting in errors comparable to a pixel width in the infrared images), it was necessary to perform a final registration step. The required position offset of the infrared image, $(\Delta\alpha, \Delta\delta)$, was estimated by minimizing the sum of squares of residuals, $\phi(\Delta\alpha, \Delta\delta, q)$, defined by

$$\phi(\Delta\alpha, \Delta\delta, q) = \sum_{\alpha,\delta} [I_{20\,\mathrm{cm}}(\alpha, \delta) - q^{-1} I_{60}(\alpha - \Delta\alpha, \delta - \Delta\delta)]^2 , \quad (1)$$

where $I_{20\,\mathrm{cm}}(\alpha, \delta)$ and $I_{60}(\alpha, \delta)$ represent the intensity distributions at wavelengths 20 cm and 60 μm, respectively, as a function of right ascension α and declination δ, and q is a scaling factor representing the weighted-mean ratio of infrared to radio intensity. The summation was performed over all positions which fell within a rectangular box, constructed so as to include the galaxy but exclude background sources.

The final numerical step was to calculate the infrared-to-radio intensity ratio, $Q_{60} = I_{60}/I_{20\,\mathrm{cm}}$, as a function of position. This quantity was then plotted, in the form of a gray-scale image, for all positions for which $Q_{60} \geq 3\sigma_Q$, where σ_Q is the standard deviation in Q. The quantity σ_Q was determined by the noise levels in the infrared and radio images, which were dominated by the dynamic ranges of the processed radio maps, typically 70:1.

4. PLOTS OF Q_{60}, AND ASSOCIATED DISCUSSION

Figures 1*a*–1*d* (Plates 15–18) show the results for all 25 galaxies, in the form of plots of Q_{60}, each of which is shown alongside a plot of infrared surface brightness, I_{60}. The peak value of Q_{60} on each plot (denoted Q_{peak}) is listed in Table 1. Examination of the plots shows that in nearly all cases, there is a local maximum in Q_{60} coincident with the galactic nucleus, as found by BH90. The principal exceptions to this behavior were IC 10 (an irregular galaxy) and NGC 3031 (a disk galaxy with a strong Seyfert nucleus), neither of which was expected to fit the model. In order to illustrate different aspects of the behavior of Q_{60}, we have plotted the data in the form of histograms, azimuthally averaged profiles, and scatter plots. For each of these plots, points which fell within 1 beamwidth (1′) of a confusing point source on the radio maps (as identified by Condon 1987) were excluded.

4.1. *Histograms*

Histograms of Q_{60} values for each galaxy are presented in Figure 2. The frequency of occurrence of Q_{60} in the histograms has been weighted by radio intensity, so that the resulting

TABLE 1

Q_{60} DATA AND RELATED PARAMETERS

Galaxy	i	Q_{peak}	l_{disk}	l_{disk}/l_Q	$(l_{\mathrm{disk}}/l_Q)_{\mathrm{BH90}}$
IC 10.....	33°	542	...	...	...
NGC 55	78	333	2.'667	0.175	0.267
NGC 253	73	497	1.715	0.188	0.183
NGC 628	21	484	1.087	0.317	...
NGC 891	78	136	0.933	0.016	...
NGC 1097.....	45	152	0.919	0.142	0.105
NGC 1569.....	59	145	0.393	0.053	...
NGC 2403.....	52	478	2.497	0.166	...
NGC 2903.....	58	173	0.656	0.101	0.043
NGC 3031.....	57	860	2.530	0.305	...
NGC 3344.....	20	176	0.679	0.194	0.062
NGC 3556.....	72	181	0.797	0.140	0.143
NGC 3261.....	49	262	0.779	0.327	0.068
NGC 4254.....	27	136	0.465	0.209	0.045
NGC 4303.....	24	311	0.511	0.436	0.045
NGC 4490.....	58	76	0.646	0.078	0.068
NGC 4565.....	80	183	1.522	0.037	...
NGC 4631.....	77	119	1.490	0.272	0.228
NGC 5055.....	52	209	0.875	0.247	0.075
NGC 5194.....	45	137	0.776	0.250	0.086
NGC 5236.....	24	242	1.031	0.306	0.141
NGC 5907.....	82	215	1.009	−0.021	...
NGC 6946.....	27	177	1.039	0.215	0.179
NGC 7331.....	68	172	1.522	0.069	...
NGC 7793.....	44	340	0.919	0.329	0.072

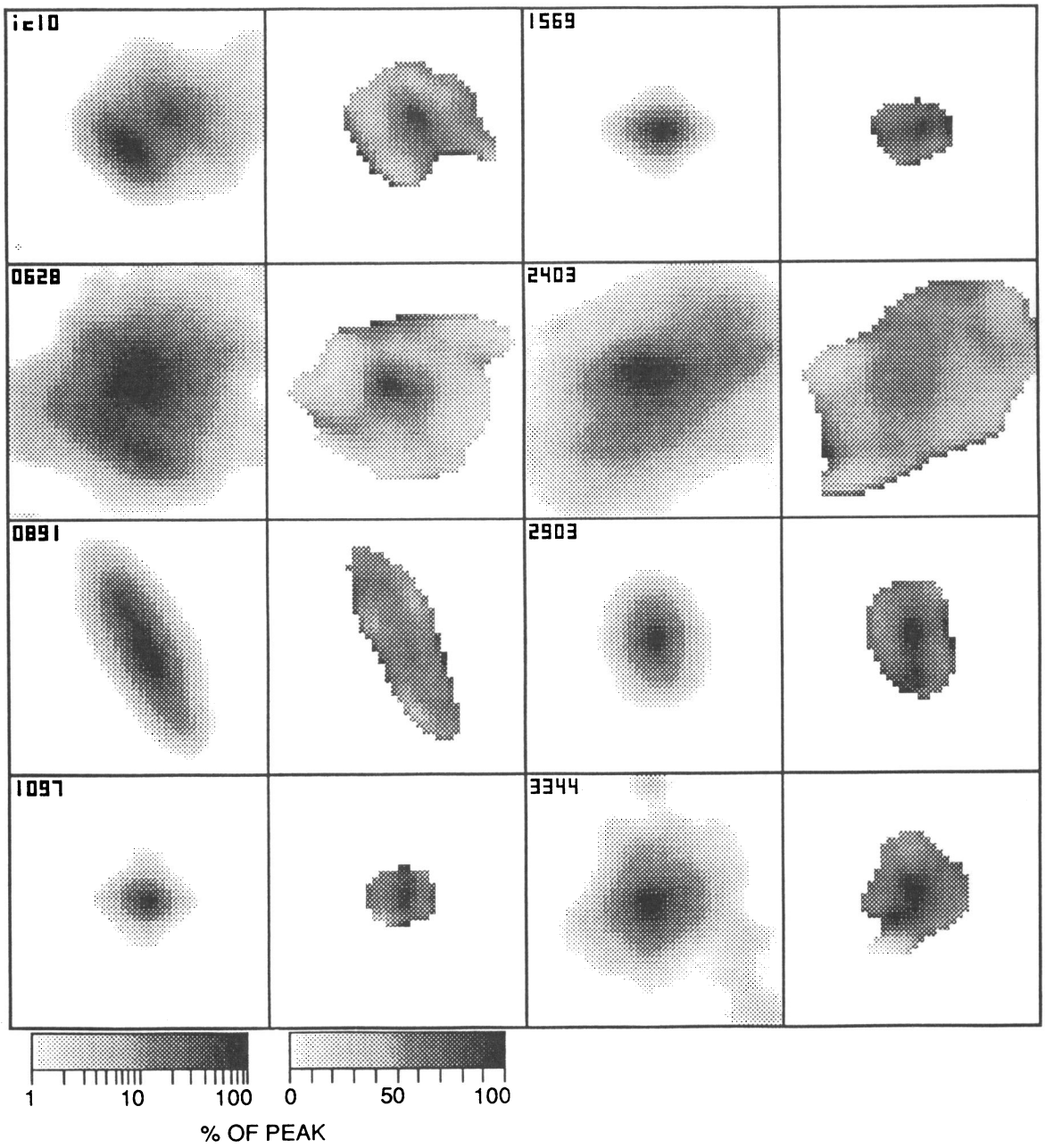

FIG. 1*a*

FIG. 1.—Spatial distribution of the 60 μm to 20 cm intensity ratio, Q_{60}. The left-hand plot of each pair represents the 60 μm infrared intensity on a logarithmic scale of 2 decades (3 decades for NGC 253); the corresponding right-hand plot shows Q_{60} on a linear scale. For (*a*), (*b*), and (*c*) the field of view is 10′ × 10′; for (*d*) it is 20′ × 20′.

PLATE 16

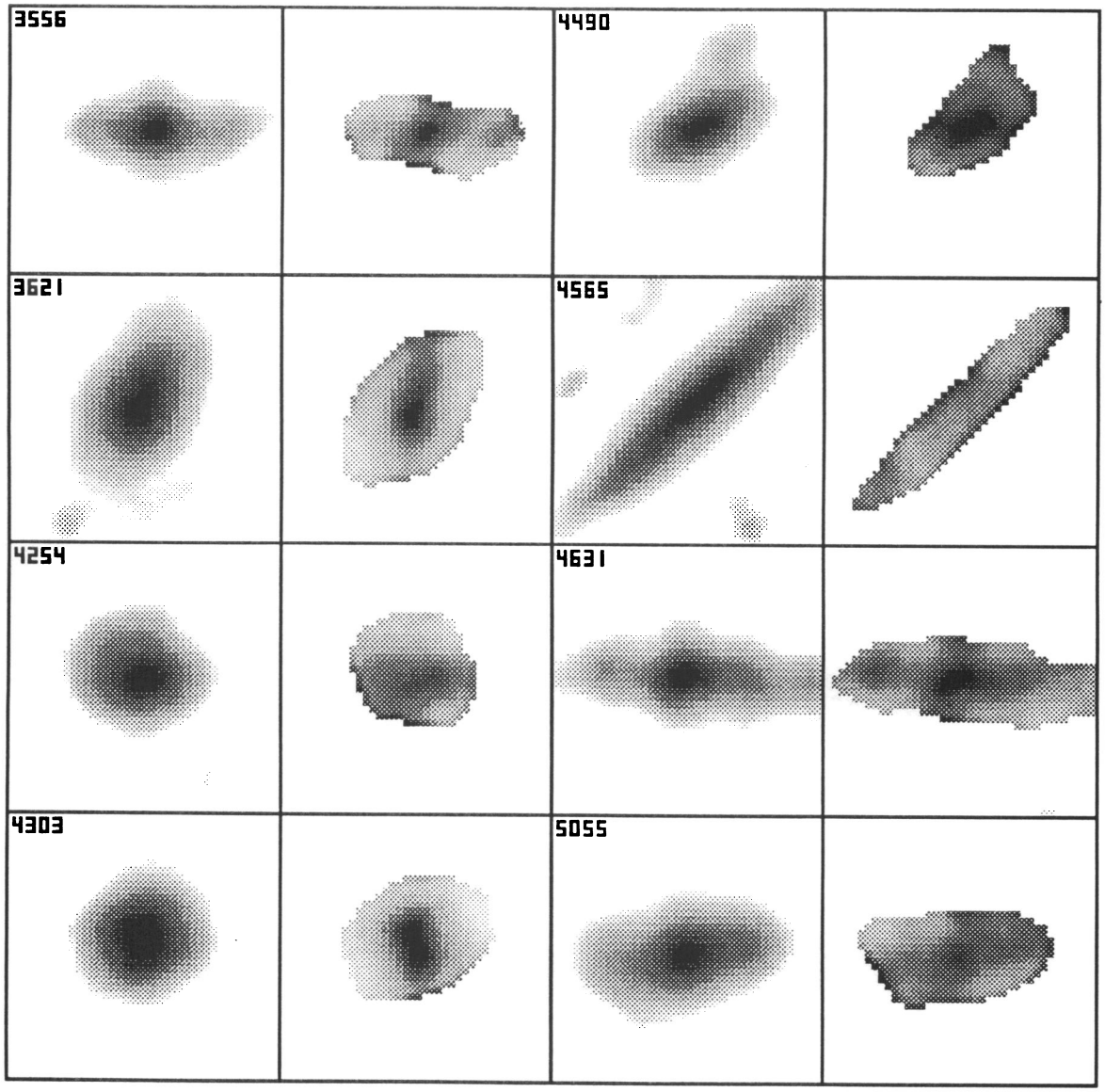

FIG. 1*b*

MARSH & HELOU (see 445, 600)

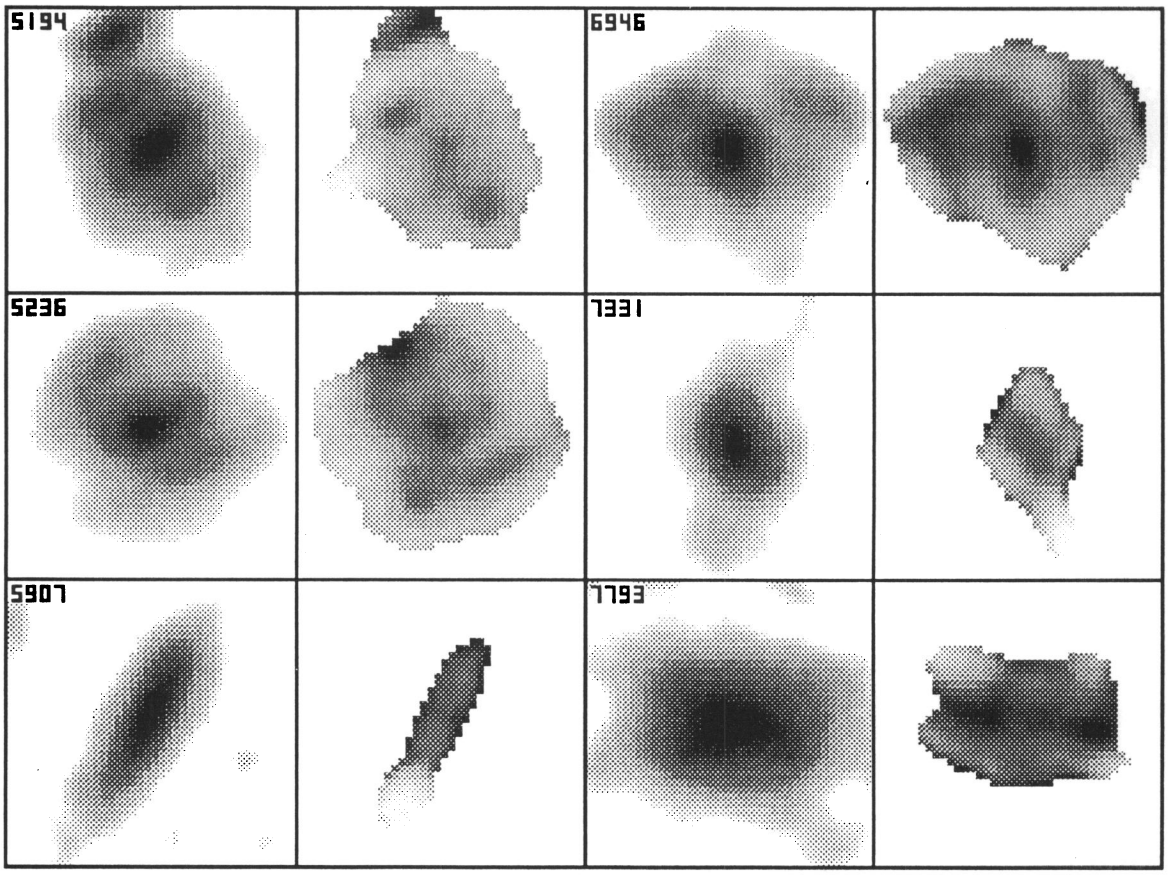

FIG. 1*c*

MARSH & HELOU (see 445, 600)

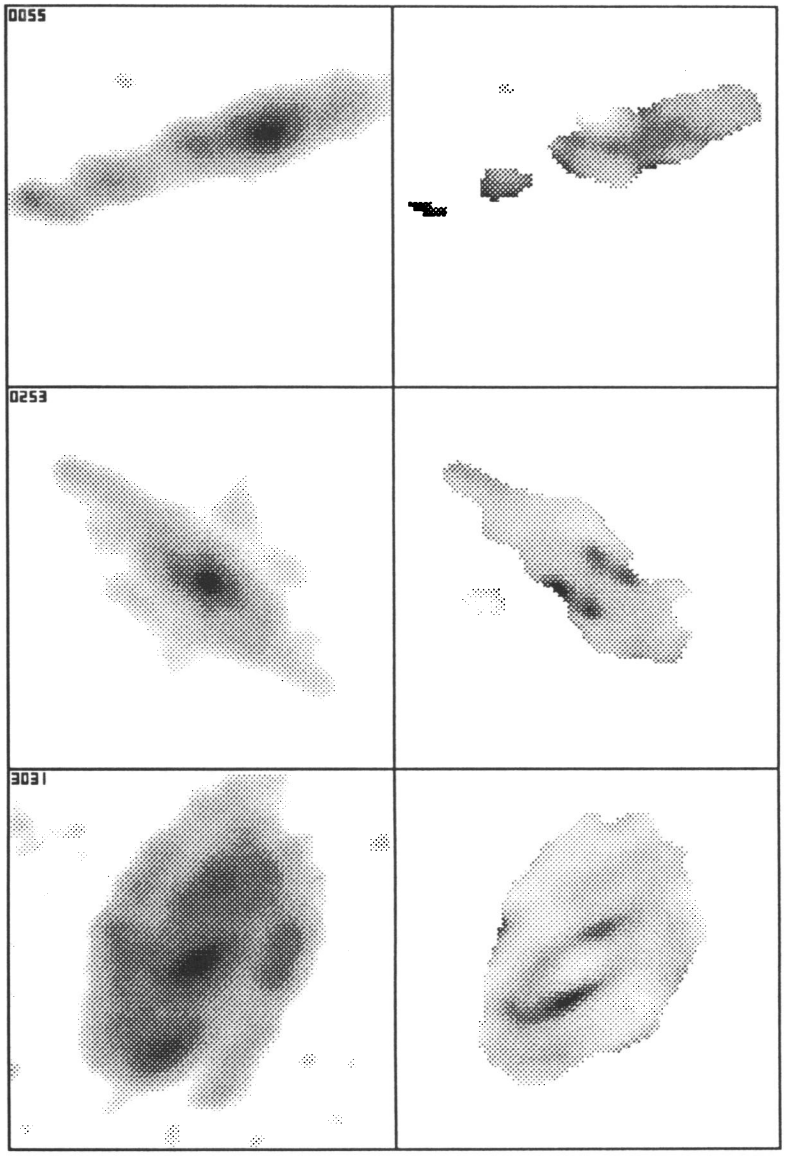

FIG. 1*d*

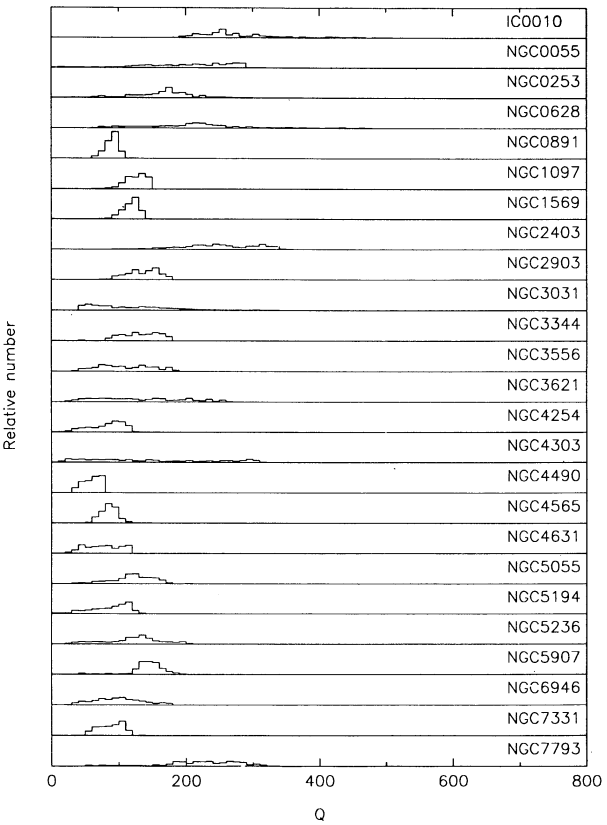

FIG. 2.—Histograms of Q_{60}, weighted by radio intensity

mean value of Q_{60} (denoted $\bar{Q}_{60}$) corresponds to the global flux ratio of 60 μm to 20 cm emission.

The histograms show that this sample of galaxies exhibits a spread of values of both the mean, $\bar{Q}_{60}$, and the width of the distribution for each galaxy. The range of $\bar{Q}_{60}$ values (100–300) is consistent with the values found by BH90. The widths of the distributions show a considerably greater range, from the narrow distributions such as NGC 891 and NGC 1569 (both of which have FWHMs of approximately 20) to the much broader distributions of galaxies such as NGC 3261 and NGC 4303, with FWHMs of approximately 200 and 300, respectively.

4.2. *Azimuthally Averaged Profiles*

Azimuthally averaged profiles of Q_{60} as a function of radial distance r from the nucleus are presented in Figure 3. The values of Q_{60} were averaged in elliptical annuli on the sky (circular in the plane of the galaxy). The nucleus was taken as the position of peak infrared intensity.

The figure shows that, in most cases, the azimuthally averaged value of Q_{60} decreases montonically with radial distance from the nucleus. One exception, already noted by BH90, is NGC 3031, whose Seyfert nucleus produces enhanced radio emission which results in a strong central depression in Q_{60}. Other exceptions are the edge-on galaxies, such as NGC 891, NGC 4565, and NGC 5907, whose Q_{60} profiles are essentially flat. The lack of Q_{60} gradients for these galaxies is reflected in the narrowness of the corresponding histograms of Figure 2, and is also quite apparent from the two-dimensional images of Figure 1. This property will be discussed further in § 5.

4.3. *Scatter Plots*

Scatter plots of Q_{60} were constructed as a function of r, and as a function of infrared surface brightness I_{60}. For these plots, the spatial sampling interval was chosen to correspond to the resolution of the images (1′ on both orthogonal axes), in order to ensure that each point represents essentially independent information. The scatter plots are presented in pairs, and are shown in Figures 4*a*–4*e*.

The interpretation of the scatter plots is aided by a comparison with the two-dimensional Q_{60} plots of Figure 1. The latter plots show that, besides the large-scale radial decrease in Q_{60}, there is, in many cases, an additional effect superposed on the general trend, in the form of off-nucleus local maxima which coincide with local maxima in I_{60}. These new details are seen in the well-resolved face-on spirals, and are particularly prominent in NGC 5194, NGC 5236, and NGC 6946. They also appear in some edge-on spirals, such as NGC 4631. These local maxima correspond to locally prominent star formation regions in the spiral arms. The new features cannot be accounted for in the simple model by Helou & Bicay (1993), which describes the I_{60} distribution as an exponential disk. They therefore partially destroy the predicted gradient of Q_{60} as a function of r. This is clearly visible in the scatter plots. The essential content, however, of the Helou & Bicay model is not in the exponential disks but in the physics of diffusion, escape, and decay of cosmic-ray electrons, and the effects on the appearance of the radio map. These effects should apply locally to each center of star formation activity, and cause the ratio Q_{60} to fall with increasing distance from each center. Since I_{60} also falls with increasing distance from a center of activity, one would expect Q_{60} and I_{60} to be positively correlated. We can test this hypothesis by comparing the scatter plots of Q_{60} versus r with those of Q_{60} versus I_{60}. The plots are consistent with our expectations, i.e., Q_{60} is more closely related to infrared surface brightness than to the radial distance in the galaxy disk.

5. ESTIMATES OF GRADIENTS

In order to make quantitative comparisons of the radial gradients of Q_{60}, the large-scale variations of I_{60} and Q_{60} in the galactic disks were represented in terms of radial exponentials with e-folding distances $\ell_{\rm disk}$ and ℓ_Q, respectively. If we denote the intrinsic (as opposed to observed) values of I_{60} and Q_{60} by $\tilde{I}_{60}$ and $\tilde{Q}_{60}$, respectively, then, on the basis of the assumed functional forms, the ratio $\ell_{\rm disk}/\ell_Q$ represents the relative radial gradient of $\ln \tilde{Q}_{60}$ with respect to the gradient of $\ln \tilde{I}_{60}$, i.e.,

$$\frac{\ell_{\rm disk}}{\ell_Q} = \frac{d \ln \tilde{Q}_{60}(r)}{dr} \Big/ \frac{d \ln \tilde{I}_{60}(r)}{dr} . \quad (2)$$

In the limit of high spatial resolution, $\ell_{\rm disk}/\ell_Q$ would also correspond to the slope of a log Q_{60} versus log I_{60} scatter plot in Figure 4, assuming that the galaxy brightnesses are well represented by radial exponentials.

The observed data were used to obtain maximum-likelihood estimates of $\ell_{\rm disk}$ and ℓ_Q. The $l_{\rm disk}$ estimates took account of the point-spread function, using a measurement model of the form

$$I_{60}(\boldsymbol{r}) = [I_0 \exp(-r/r_0)] * h(\boldsymbol{r}) + \xi(\boldsymbol{r}) , \quad (3)$$

where

$$r_0 = l_{\rm disk} \cos i/[1 - (x \sin\theta + y \cos\theta)^2 \sin^2 i/r^2]^{1/2} , \quad (4)$$

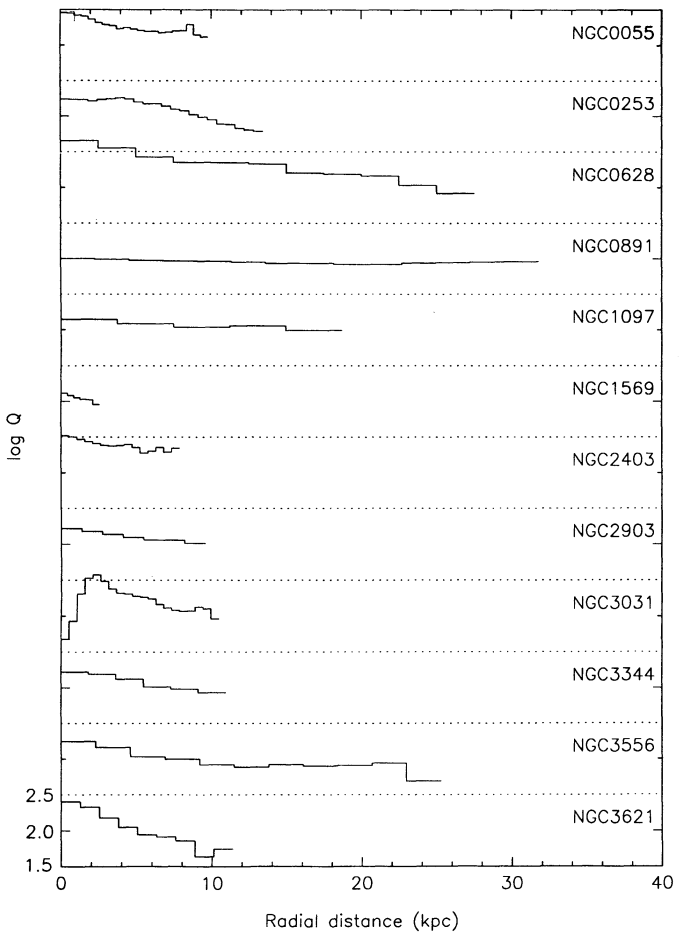

FIG. 3a

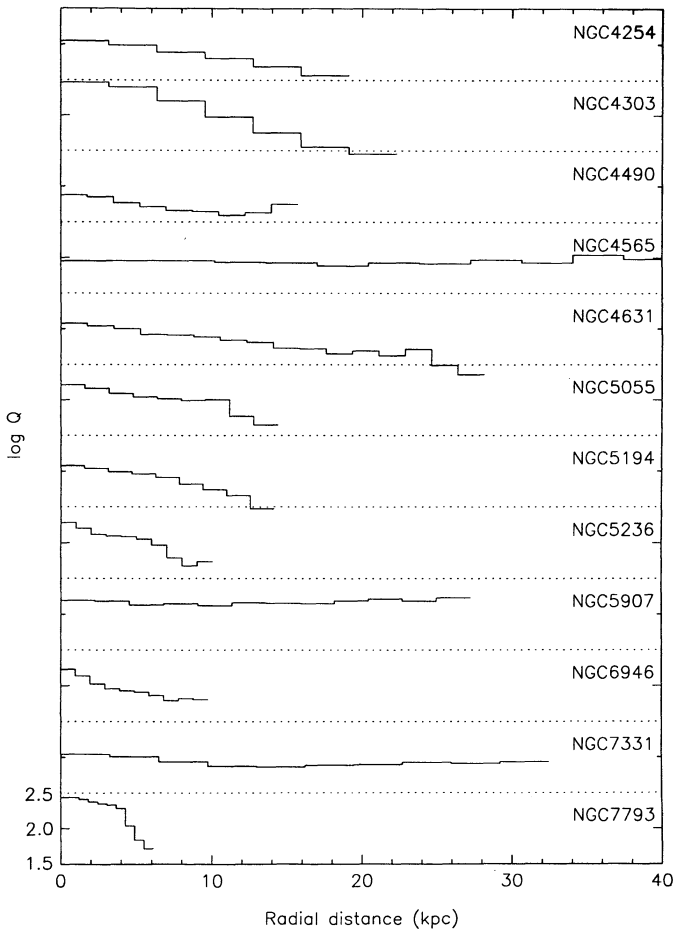

FIG. 3b

FIG. 3.—Radial profiles of $\log Q_{60}$, averaged in elliptical annuli (the projections of circular annuli in the disk plane) of width 2 pixels (0.5)

such that $\boldsymbol{r}$ is a two-dimensional angular position vector of magnitude $r = (x^2 + y^2)^{1/2}$, where x and y represent the right ascension and declination offsets from the galactic nucleus, i and θ are the inclination and position angle of the tilt axis of the galactic disk, respectively, $h(\boldsymbol{r})$ is the point-spread function, and the asterisk represents convolution. The quantity $\xi(\boldsymbol{r})$ is a random variable representing a combination of model error and measurement noise. It is assumed to be a zero-mean Gaussian process whose standard deviation is proportional to I_{60}. The latter condition ensures that shape information contained in the low-intensity portion of the disk receives as much weight as that of high-intensity features such as the nucleus and inner disk.

Estimation of ℓ_Q, with similar allowance for the point-spread function, would be complicated by the fact that the measured Q_{60} values are not related to the true values by simple convolution. Therefore, a simpler procedure was adopted, in which the estimates of ℓ_Q were made using simple least-squares fits of $\ln Q_{60}$ as a function of r, using the data from the radial plots of Figure 3.

The results of the fits are presented in Table 1, in the form of the estimated values of $\ell_{\rm disk}$ and $\ell_{\rm disk}/\ell_Q$. Next to the $\ell_{\rm disk}/\ell_Q$ values are the corresponding values from BH90, for comparison. Also included in the table are the values of the inclination i of the disk with respect to the plane of the sky, taken from BH90. The irregular galaxy IC 10 was not included in this part of the analysis, since it does not provide a meaningful fit to an exponential disk. In the case of NGC 3031, the central portion was omitted from the fit because of the effects of the enhanced radio emission from the Seyfert nucleus. It is apparent from the values of $\ell_{\rm disk}/\ell_Q$ that Q_{60} falls off much more slowly than the brightness of the disk, in agreement with BH90. However, it is also apparent that in more than half of the cases, the present values of $\ell_{\rm disk}/\ell_Q$ are significantly larger than those obtained by BH90. The discrepancy lies in the values of ℓ_Q rather than those of $\ell_{\rm disk}$, and we attribute it to spatial dilution effects in the BH90 data, for reasons which will be discussed below.

Figure 5 shows a plot of the relative radial gradient, $\ell_{\rm disk}/\ell_Q$, versus the inclination of the galaxy, using the data from Table 1. The plot shows a distinct, albeit weak, correlation between these two quantities, in the sense that the relative radial gradient decreases with increasing inclination. At one end of this trend are the edge-on galaxies which show no apparent Q_{60} gradient.

The trend can be understood in terms of the line-of-sight superposition of the off-nucleus emission regions discussed in § 4.3. Specifically, the greater the inclination of the galaxy, the greater the number of separate emission regions which become averaged, within the instrumental beam, along the line of sight, and hence the greater will be the dilution of the Q_{60} gradients associated with each such region. We have tested the plausibility of this hypothesis by simulating the appearance of

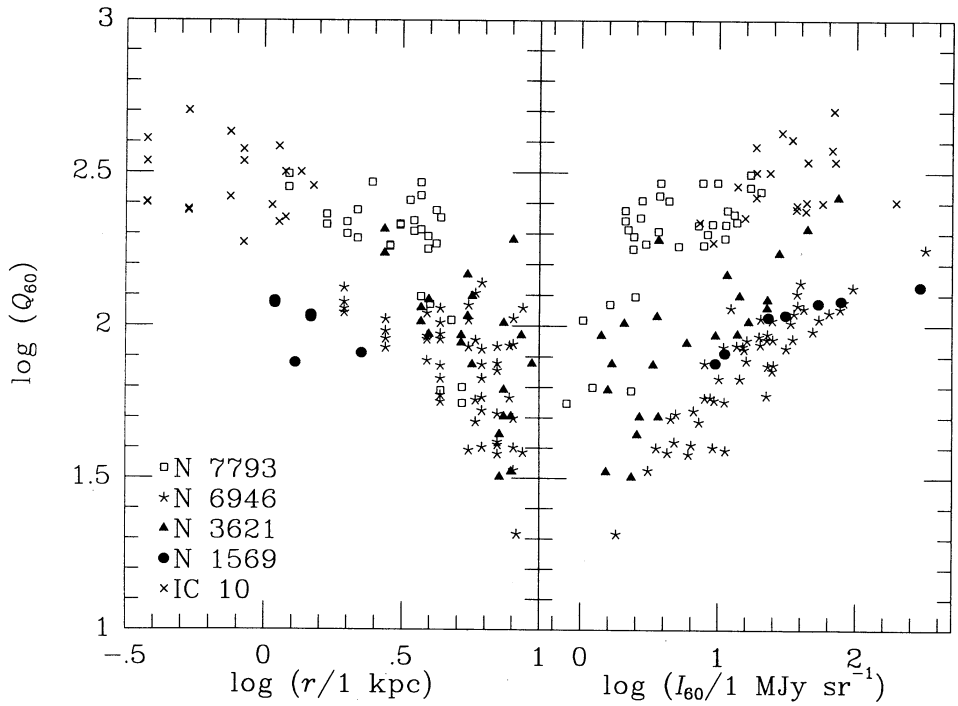

FIG. 4*a*

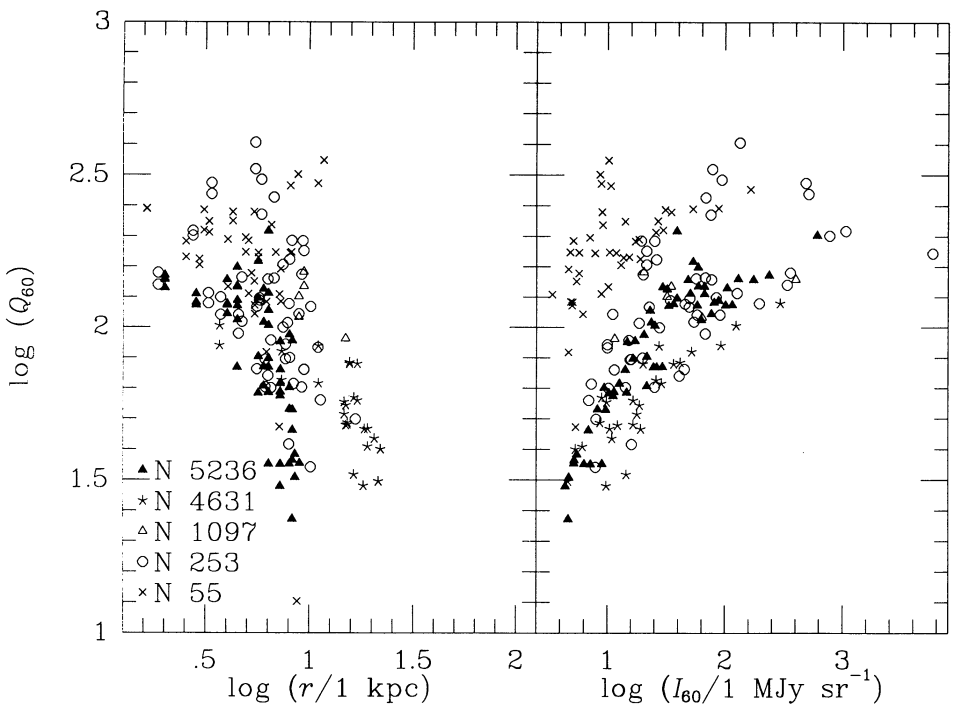

FIG. 4*b*

FIG. 4.—Scatter plots of Q_{60} as a function of radial distance r from the nucleus and infrared surface brightness I_{60}

edge-on galaxies using one-dimensional "fan-beam" averages of nearly face-on galaxies and examining the corresponding spatial behavior of Q_{60}. This was carried out for the nine galaxies with $i \leq 45°$; fan-beam averages were constructed in two orthogonal directions for each galaxy, making a total of 18 cases. The results have been plotted in Figure 5, which shows that for each of the nine galaxies, the effect of fan-beam averaging was to reduce the radial gradient. We therefore conclude that the above trend with inclination can be explained by contrast dilution resulting from line-of-sight superposition.

Contrast dilution also provides an explanation for the fact that the presently estimated Q_{60} gradients tend to be larger than those of BH90. The reason is that the spatial resolution in the latter study was much poorer along one axis, resulting

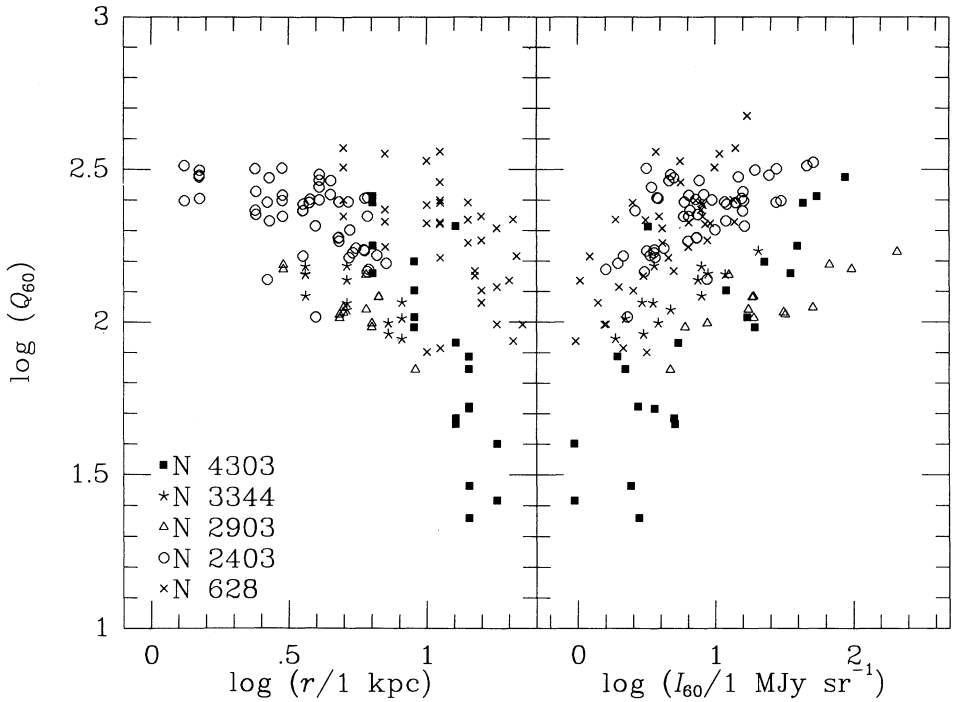

FIG. 4*c*

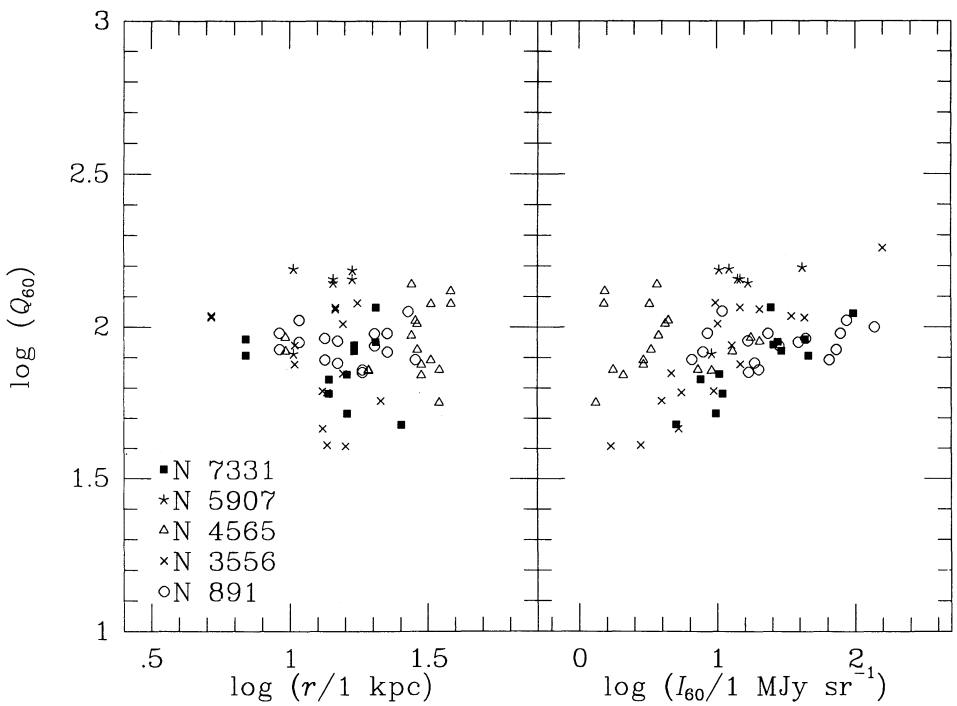

FIG. 4*d*

effectively in fan-beam averaging along that axis, with consequences similar to line-of-sight superposition.

6. ARE THE OBSERVED Q_{60} GRADIENTS REAL?

Could the radial gradients in Q_{60} be spurious effects induced by the data reduction? In considering this question, it is important to note that the rectification procedure described in § 3 was carefully designed to ensure that both the radio and infrared maps possessed the same spatial resolution, so that any observed differences could be attributed to real differences in source structure. It assumed, of course, that the instrumental resolution was known accurately for both radio and infrared. We believe that this is a good assumption, since (*a*) the spatial resolution of the radio images is determined by the physical spacing of the interferometer dishes and by the width of the restoring beam, both of which are known accurately, and (*b*)

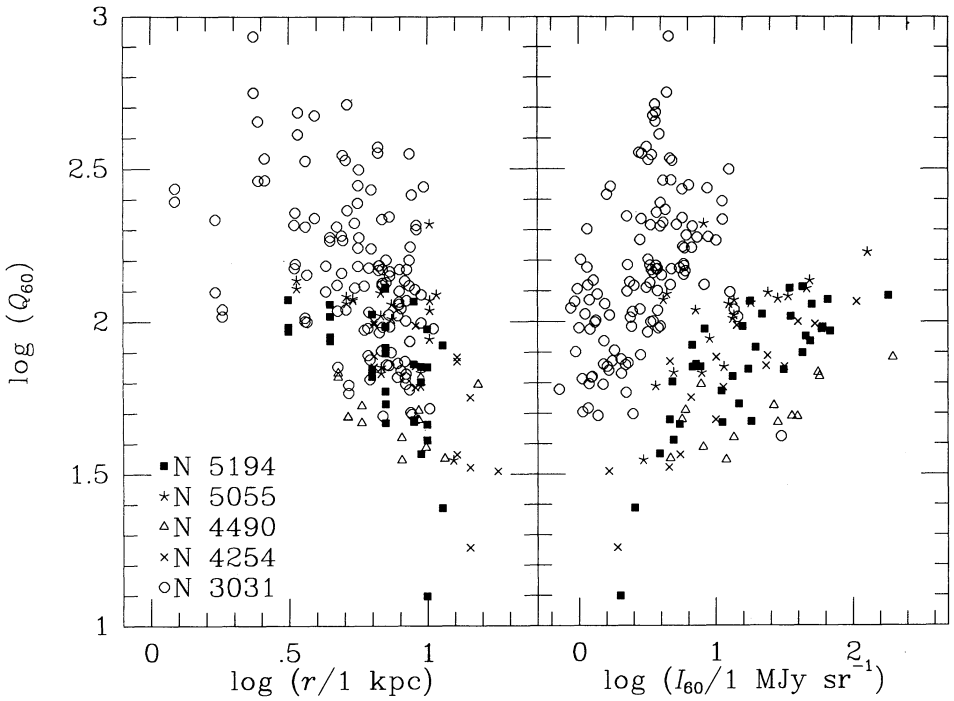

FIG. 4*e*

the *IRAS* detector responses have been carefully measured using observations of point sources (*IRAS* Explanatory Supplement 1988). The only known source of systematic error in the latter is a truncation of the response at ~1% of maximum. This error would cause infrared sources to appear slightly broader than they actually are, which would have the effect of *reducing* any radial gradients in Q_{60}. Thus this error would not be capable of producing spurious gradients.

Perhaps the best piece of independent evidence for the reality of the radial gradients is that some galaxies do not show the effect at all. If the gradients were simply a result of the radio images possessing more instrumental smearing than the infra-

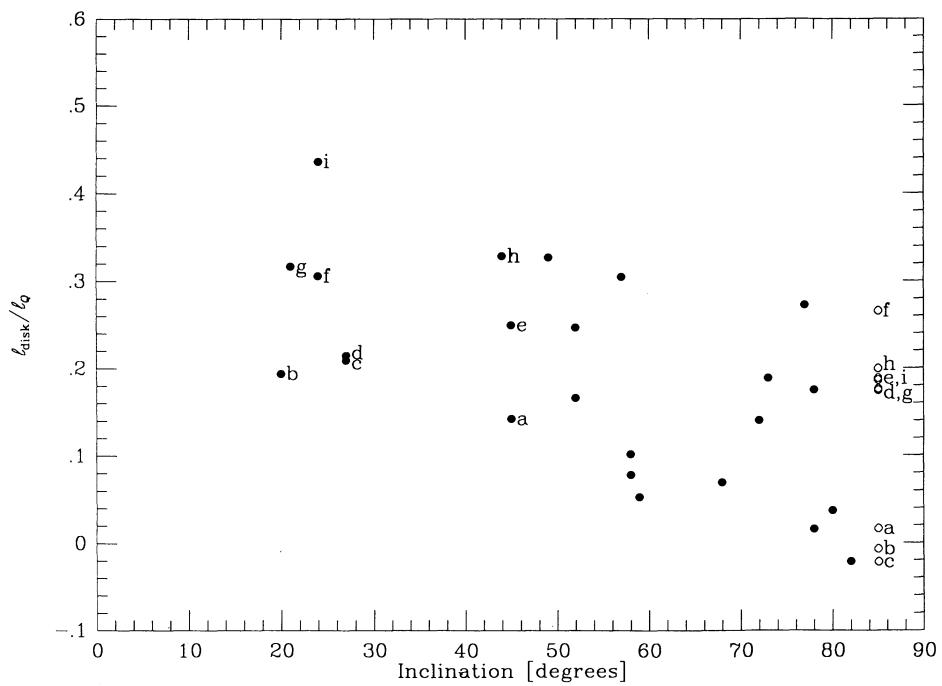

FIG. 5.—Relative radial gradient of ln Q_{60} (represented by ℓ_{disk}/ℓ_Q) as a function of the inclination of the disk of the galaxy. The filled circles represent values estimated from the two-dimensional images. The open circles represent simulated values for edge-on galaxies (whereby structure becomes averaged along the line of sight) and were obtained from fan-beam averages of the low-inclination galaxies ($i \leq 45°$). Each open circle represents the mean of the two values obtained from orthogonal averaging directions, and is labeled to enable comparison with the original value, i.e., *before* fan-beam averaging (the corresponding filled circle).

red images, then all of the compact infrared sources on the images (e.g., the galactic nuclei) would correspond to similar local radial decreases in Q_{60}. The fact that some galaxies (e.g., NGC 891, NGC 4565, and NGC 5907) shown no Q_{60} gradients while others (e.g., NGC 4303 and NGC 6946) show a prominent falloff from the nucleus, strongly supports a noninstrumental origin for the gradients.

A piece of statistical evidence for the reality of the gradients is that the Q_{60} gradients appear to be systematically suppressed for the high-inclination galaxies. Since the calculation of the two-dimensional Q_{60} images involved no assumptions about inclination, this argues for an astrophysical origin for the gradients.

7. CONCLUSIONS

The two principal conclusions from the study are the following:

1. The previously reported gradients in Q_{60} are real, i.e., the close proportionality of total flux densities in infrared and radio is not, in general, maintained locally within galaxies.

2. Although azimuthally averaged plots of Q_{60} show a monotonic decrease with radial distance from the nucleus, the detailed two-dimensional behavior of Q_{60} shows the presence of off-nucleus local maxima, coincident with local maxima in infrared intensity. Each such local maximum probably represents a separate site of star formation activity, and behaves as a local center from which Q_{60} decreases radially.

The behavior of Q_{60} in the vicinity of each of the local emission centers is in qualitative agreement with the suggestion (BH90) that the radio image represents a smeared version of the infrared image. This suggestion will be examined quantitatively in a forthcoming paper in which the radio images will be compared with convolved versions of the infrared images, using various smearing kernels.

As the spatial resolution of the images is increased in future observations, we expect that a point will be reached at which structural details of the confining magnetic field are resolved, and the convolutional relation will begin to break down. In the case of NGC 253, the mid-IR and radio become decorrelated on spatial scales below about 100 pc (Keto et al. 1993). If this scale is representative of the far-IR also, then the spatial resolution of the present images is an order of magnitude too coarse to show such effects. We therefore expect the convolutional relation to be maintained, and will attempt to verify this in our upcoming paper.

We thank an anonymous referee for helpful suggestions. We also thank Nanyao Lu, J. W. Fowler, and B. Wells for their comments on the manuscript; M. D. Bicay and Zhong Wang for stimulating discussions; and D. Engler for running the MCM software. This research has been supported through the *IRAS* Extended Mission Program by the Jet Propulsion Laboratory, California Institute of Technology, under contract with the National Aeronautics and Space Administration.

REFERENCES

Aumann, H. H., Fowler, J. W., & Melnyk, M. 1990, AJ, 99, 1674
Beck, R., & Golla, G. 1988, A&A, 191, L9
Bettens, R. P. A., Brown, R. D., Cragg, D. M., Dickenson, C. J., & Godfrey, P. D. 1993, MNRAS, 263, 93
Bicay, M. D., & Helou, G. 1990, ApJ, 362, 59 (BH90)
Bicay, M. D., Helou, G., & Condon, J. J. 1989, ApJ, 338, L53
Condon, J. J. 1987, ApJS, 65, 485
de Jong, T., Klein, U., Wielebinski, R., & Wunderlich, E. 1985, A&A, 147, L6
Dickey, J. M., & Salpeter, E. E. 1984, ApJ, 284, 461
Helou, G., & Bicay, M. D. B. 1993, ApJ, 415, 93
Helou, G., Soifer, B. T., & Rowan-Robinson, M. 1985, ApJ, 298, L7
IRAS Catalogs and Atlases: Explanatory Supplement. 1988, ed. C. A. Beichman, G. Neugebauer, H. J. Habing, P. E. Clegg, & T. J. Chester (Washington, DC: GPO)
Karoji, H., Dennefeld, M., & Ukita, N. 1985, A&A, 155, L3
Keto, E., Ball, R., Arens, J., Jernigan, G., Meixner, M., Skinner, C., & Graham, J. 1993, ApJ, 413, L23
Price, R., & Duric, N. 1992, ApJ, 401, 81
Sanders, D. B., & Mirabel, I. E. 1985, ApJ, 298, L31
Wainscoat, R. J., de Jong, T., & Wesselius, P. R. 1987, A&A, 181, 225
Wrobel, J. M., & Heeschen, D. S. 1988, ApJ, 335, 677
Wunderlich, E., & Klein, U. 1988, A&A, 206, 47